Experiences in the synthesis and Exploitation of Nanomaterials

B.Viswanathan, P.S.Kishore, J.Rajeswari and T.K.Varadarajan
National Centre for Catalysis Research
Indian Institute of Technology, Madras

Abstract
Some of the synthesis strategies employed for the design and formation of functional nanomaterials are outlined. The potential uses of these nano materials have also been examined.

Introduction

The desire to synthesize nanostructured materials that can exhibit high performance in several electrochemical applications by utilizing the unique properties of nanomaterials and high electrical conductivity and catalytic activity of metal oxide cluster compounds (polyoxometalates) and their parent metal oxides (M= W, Mo and V) has inspired and motivated the development of techniques for the fabrication of (i) metal nanoparticles supported on carbon, (ii) 1-D nanorods and (iii) metal nanoparticle-polyoxometalate-conducting polymer composites. Nanotechnology brings new possibilities for developing novel electrocatalysts and electrode systems. Modification of electrode surfaces with nanomaterials such as metal nanoparticles [1], 1-D nanostructures such as nanorods, nanotubes, nanowires [2-3] has recently received a considerable interest as a consequence of the rapid progress in nanotechnology both in fundamental and technological applications. In general, and compared with their bulk materials, nanomaterials, with their size, morphology, large specific surface area and possible quantum confinement, exhibit unique physical and chemical properties. Hence, these advantages can be added onto the electrode surfaces. In addition to this, dimensionality have also been found to play a critical role in determining the properties of materials due to the different ways that electrons interact in three dimensional, two-dimensional and one-dimensional structures [4]. Hence, there has been a continous interest in studying the dimensionality-dependent properties of materials and ultimately to fabricate nanodevices. In general,

noble metals or metal containing compounds, such as Pt, RuO_2 are employed as electrodes or electrocatalysts for several electrochemical applications such as methanol oxidation [5,6], Hydrogen Evolution Reaction [7, 8], Oxygen Reduction Reaction (ORR) [9, 10] and electrochemical supercapacitors [11-13]. Hence, the current work aims at two possibilities. Firstly, to reduce the loading of noble metals by employing electrocatalysts based on polyoxometalates (POM) or tungsten trioxide nanorods (WO_3). This strategy was effectively used for electrochemical applications such as methanol oxidation, oxygen reduction reaction, electrochemical supercapacitors and hydrogen evolution reaction. The second one aims at replacing the noble metal oxides by low cost metal oxides for electrochemical supercapacitor applications. This has been achieved by employing tungsten trioxides as materials for electrochemical supercapacitors. The electrocatalysts based on polyoxometalates (POM) and tungsten trioxide nanorods (WO_3) were synthesized with the idea of incorporation of value adding properties of POMs such as fast electron transfer ability, enhanced availability and mobility of protons at the interface, high electron conducting behavior due to the hydrogen bronzes formed in the presence of acid, stability offered to the metal nanoparticles [14-17].

Experimental

Materials

Silicotungstic acid (STA), hexachloroplatinic acid and ruthenium (III) chloride hydrate were procured from Sigma-Aldrich and used as received. Carbon Black (Vulcan XC-72R, Cabot) with specific surface area (BET) of 250 m^2g^{-1} was used as the carbon support for all the catalysts. The commercial tungsten trioxide (bulk WO_3) was purchased from Alfa Aesar. All other chemicals were purchased from Sisco Research Laboratories Pvt. Ltd and used as received.

Characterization

X-Ray Diffraction (XRD) patterns were obtained by a powder diffractometer (XRD - SHIMADZU XD-D1) using a Ni-filtered CuKα X-ray radiation source. CRM 200 Raman spectrometer was employed, using the 514.5 nm line of an Ar ion laser as the excitation source. Scanning electron microscopic images were obtained from FEI, Model: Quanta 200. Transmission electron microscopy (TEM), Electron diffraction and Energy Dispersive X-ray Analysis (EDAX) were performed on a Philips CM12/STEM

instrument. High-resolution Transmission Electron Microscopy (HRTEM) was carried out on a JEOL 3010.

Electrochemical Characterization

A three electrode cell consisting of the glassy carbon as working electrode (0.07 cm^2), Pt wire and Ag/AgCl (satd. KCl) electrodes as counter and reference electrodes respectively were used. All electrochemical measurements were performed using a CHI660A potentiostat/galvanostat. The working electrodes for electrochemical measurements were fabricated by dispersing 5 mg of the catalyst in 100 µl of deionized water by ultrasonication for 20 min. From this dispersion 10 µl has been taken and placed on a glassy carbon electrode. The solvent was slowly evaporated by placing the electrode in an oven at 70 °C. 5 µl of nafion solution has been coated on the electrode as a binder and dried at room temperature. 1M H_2SO_4 was used as the electrolyte. The electrolyte solution was deaerated with high purity N_2 (99.99%) for 30 min before the electrochemical measurements.

Synthesis

1. Synthesis of Pt and Pt-Ru supported on carbon (Pt/STA-C and Pt-Ru/ STA-C) by POM reduction method (communicated)

The typical procedure involved the following steps. Specific amounts of hexachloroplatinic acid (10mM) or hexachloroplatinic acid (10mM) and ruthenium (III) chloride hydrate (10mM) have been loaded on carbon to get 20 wt% metal loading by conventional impregnation method. The composition of Pt and Ru was fixed to produce a final atomic ratio of 1:1 in the preparation of all Pt-Ru based composite catalysts. The mixture has been magnetically stirred for 3h at room temperature and then evaporated to dryness at 80° C. Reduced silicotungstic acid (represented either as STA or SiW_{12}) (10mM) has been added to the impregnated material, followed by microwave irradiation for 90 s. The color of the reduced STA has changed from blue to colorless indicating the oxidation of STA, ensured the electron transfer from STA to metal ions. This electron transfer functions because of the lower potential of the one equivalent reduced tungstate couple $[SiW_{12}O_{40}]^{4-}$/ $[SiW_{12}O_{40}]^{5-}$ (0.057 V vs. NHE; NHE = Normal Hydrogen Electrode) relative to ($PtCl_6^{2-}/Pt^0$) 0.725 V vs. NHE). Facile electron transfer drives the reduction of metal ions. The final solid products of 20% Pt/STA-C and 20% Pt-Ru/STA-

C were obtained by centrifugation, washed with water and then dried in vacuum at 70 °C for 8h.

1.1 Preparation of STA free Pt and Pt-Ru supported on carbon (Pt/C and Pt-Ru/C) by hydrogen reduction method (communicated)

For comparison, a second set of catalysts, 20% Pt/C and 20% Pt-Ru/C have been prepared by impregnation method with similar composition as mentioned above. The resultant material was then introduced into a tubular furnace and reduced under flowing H_2 gas at 350 °C for 3 h.

2. Synthesis of Ru supported on carbon (Ru/ SiW_{12}-C) by POM reduction method (P. S. Kishore, B. Viswanathan and T. K. Varadarajan, Indian Pat. Appl.)

Impregnation of Ru nanoparticles on carbon by POM reduction method has been carried out by wet impregnation method. Specific amounts of hexachloroplatinic acid (10mM) or hexachloroplatinic acid (10mM) and ruthenium (III) chloride hydrate (10mM) have been loaded on carbon to get 10, 20 and 40 wt% metal loading by conventional impregnation method. Reduction of the impregnated metal on carbon support to its metallic state was performed by the addition of reduced POM solution and simultaneous irradiation with microwave radiation by placing the vessel in a domestic microwave oven operating at a frequency of 2450 MHz (power 700 W) for 1 min. The unadsorbed polyoxometalates was removed by washing with water and ethanol and by centrifuging at a speed of 10, 000 rps. The final product was obtained by drying the sample under vacuum at room temperature for 12h.

3. Preparation of Ag (silver) -PANI (polyaniline) -PMo_{12} (phosphomolybdic acid) nanocomposite (communicated to *Nanoscale Research Letters*)

Aniline was polymerized by slow addition of phosphomolybdic acid PMo_{12}) at room temperature to which metal salt solution has been added immediately and ultrsonicated for 5 min. For a typical synthesis 600 μL of 50mM PMo_{12} aqueous solution has been added slowly to 100 μL of aniline at room temperature, immediate change in the color of the solution to blue was observed. Aniline was oxidized to polyaniline by transferring

electrons to PMo12. The reduced PMo12 formed during polymerization is responsible for the blue color. To the resultant solution 10mM aqueous solution of AgNO3 has been added and ultrasonicated for 5 min, the resulting mixture was allowed to stand without stirring for 24h. The as prepared sample (Ag-PAni-PMo_{12}) was filtered out, washed and dried under vacuum. The similar strategy was also employed for the preparation of Au nanoparticles embedded PAni (Au-APni-PMo_{12}) by the addition of 10 mM $HAuCl_4$ instead of $AgNO_3$ in the above mentioned procedure.

4. Synthesis of 1-D Metal oxide (M= W, Mo and V) and MoS_2 nanorods

4.1 Synthesis of WO_3 nanorods

(J. Rajeswari, B. Viswanathan and T. K. Varadarajan, Tungsten trioxide nanorods as supports for platinum in methanol oxidation, Materials Chemistry and Physics, 2007 (in press))

Tungsten trioxide nanorods have been synthesized by using tetrabutylammonium decatungstate as the precursor material. The starting material was prepared according to the work described elsewhere [60]. The typical procedure involved the precipitation of tetrabutylammonium decatungstate by adding an aqueous tetrabutyl ammonium bromide solution to a clear yellow solution of tungstic acid preformed using sodium tungstate and concentrated hydrochloric acid. The white precipitate was washed with boiling water and ethanol, filtered, dried and then recrystallized in hot dimethyl formamide to give yellow crystals. The thermogravimetric analysis revealed that the tetrabutylammonium cation content in the compound is 29.0 % (theoretical value: 29.2 %) and the decomposition temperature is around 450° C as reported [60]. The synthesis of tungsten trioxide (WO_3) nanorods from tetrabutylammonium decatungstate ($((C_4H_9)_4N)_4W_{10}O_{32}$) is carried out as follows: The precursor compound (1g) was taken in an alumina or quartz boat and loaded inside a tubular furnace and heated at 450º C at a heating rate of 25º C per min under Ar atmosphere for 3h. This was followed by gradual cooling to room temperature to obtain a blue powder of WO_3 nanorods. The total yield of the obtained material was 71% by weight (relative to the starting material). To further investigate the role of tetrabutylammonium (TBA) group on the morphology of WO_3, an experiment has been carried out in the absence of tetrabutylammonium ion. To achieve this, $(NH_4)_{10}H_2W_{12}O_{42}.XH_2O$ has been taken as the precursor and pyrolysed under similar

experimental conditions that were employed for the formation of WO_3 nanorods (our refs).

4.2 Synthesis of electrocatalysts for methanol oxidation and ORR (Pt /WO_3 and Pt/ WO_3-CNT or Pt/ WO_3-C) (Results unpublished)

To load 20 % Pt on support (WO_3, WO_3-CNT and C (Vulcan XC72R)), wet impregnation method was adopted wherein 0.01 M aqueous hexachloroplatinic acid (H_2PtCl_6) was mixed with required amount of the support by stirring at room temperature. It was then evaporated to dryness followed by reduction in hydrogen atmosphere at 350° C - 450 ° C for 4h.

4.3 Synthesis of MoO_2 and MoS_2 nanorods (Results unpublished)

Tetrabutyl ammonium salt of molybdic acid was taken in an alumina or quartz boat and loaded in a tubular furnace and pyrolysed at 700º C to obtain MoO_2 nanorods respectively. An alumina boat containing tetrabutyl ammonium salt of molybdic acid was placed in a tubular furnace and heated at 800º C in Ar atmosphere for 30 min and H_2S gas for 30 min to form MoS_2 nanorods.

2.3 Synthesis of $Mo_xV_yO_z$ nanorods

Tetrabutyl ammonium salt of phosphomolybdovanadic acid was taken in an alumina or quartz boat and loaded in a tubular furnace and pyrolysed at 750º C to obtain $Mo_xV_yO_z$ nanorods respectively.

Results and Discussion

1. Pt/STA-C and Pt-Ru/STA-C (communicated)

A schematic illustration of the preparation of Pt/STA-C composite is given in Scheme. 1. The carbon source has been impregnated with hexachloroplatinic acid to get the Pt metal ions loaded carbon. In order to reduce and stabilize the metal ions on the carbon support, reduced STA (blue colored species) has been added and simultaneously irradiated with microwave radiation. The blue color of the solution changed to colorless indicating the

oxidation of STA. For comparison, the Pt or Pt-Ru loadings in all the composites were done at the nominal Pt level in the commercial catalyst, i.e., 20 wt% of Pt or Pt-Ru.

The reduction of STA has been followed by observing changes in the optical spectra of the STA in aqueous solutions as shown in Figure 1. STA (W metal in d^0 state) has no absorbance in the range of 400 -700 nm (Figure 1a). Whereas, the blue colored filtrate obtained from the mixture of STA and Zn metal powder, has an absorption band at 700 nm (Figure 1b). The produced d^1 metal ion of W is responsible for the d-d transition resulting in absorption in the visible region. This indicates the formation of reduced 'heteropoly blue' of STA.

To examine the immobilization of Pt or Pt-Ru nanoparticles on composites, transmission electron microscopy (TEM) measurements of the prepared catalysts were carried out. Representative TEM micrographs of the Pt/STA-C and Pt-Ru/STA-C can be seen in Figure 2a & 2b respectively. In both the composites the metal nanoparticles are highly dispersed on the carbon support. The particle size distribution obtained from the TEM images of Pt/STA-C and Pt-Ru/STA-C have been shown in Figure 2c & 2d respectively. A statistical analysis of the TEM image shows that Pt nanoparticles have an average diameter of 2.8 nm, with a size distribution standard deviation of 1.8 nm in the Pt/STA-C composite. Pt-Ru nanoparticles have an average diameter of 3.6 nm, with a size distribution standard deviation of 2.4 nm in Pt-Ru/STA-C composite. Pt and Pt-Ru nanoparticles on carbon support produced by the hydrogen reduction method resulted in larger particles with mean diameters of 11.7 nm and 16.5 nm in Pt/C and Pt-Ru/C composites respectively (Figure 2e & 2f). The TEM images reveal that hydrogen reduction method produces larger particles with low dispersion when compared to the POM reduction method which produced nanoparticles with small size and fine dispersion. The repulsive interaction between the like-charged POMs has the ability to prevent the agglomeration of the metal nanoparticles. The low-resolution (HRTEM) image (Figure 3a) demonstrates the dispersion of Pt nanoparticles on carbon nanobelts that are formed during the synthesis of Pt/STA-C composite. The strong and irreversible chemisorption of STA anions on the carbon surface leads to the formation of such carbon nanostructures. A relatively short microwave irradiation (90s) has driven STA to attach spontaneously to the carbon surface, as polyanions provide static repulsion on the carbon

surface; this allowed the transformation into carbon nanobelt. A similar effect has been observed by other authors, where carbon nanostructures such as carbon nanotubes, nanobelts and nanoparticles, quasi two-dimensional graphite sheets were formed by the adsorption of POM on carbon surface. The dispersion of the Pt nanoparticles on carbon nanobelts is more evident in the high resolution image (Figure 3b). The lattice fringes of the Pt and Pt-Ru nanoparticles are evident from HRTEM images of Pt/STA-C (Figure 3c) and Pt-Ru/STA-C (Figure 3d) respectively. To confirm the presence of STA and its chemisorption on the carbon surface FTIR (Figure 4a) and EDX (Figure 4b) measurements were carried out. The FTIR spectrum of pure STA shows four characteristic absorption bands at 1025, 980, 926 and 784cm^{-1} (Figure 4a(i)) ascribed to vibrations: ν_s (W-O), ν_{as}(W=O), ν_{as}(Si-O) and ν_{as} (W-O-W) respectively in the hydrated Keggin unit of STA. The presence of chemisorbed STA in the composites is evident from the FTIR spectra of Pt/STA-XC-72R and Pt-Ru/STA-C, because the unique bands of the STA have been observed (Figure 4a (ii) & (iii)). Slight shift in the ν_{as} (Si -O) bands were observed due to the adsorption on to the carbon surface. The band due to external ν_{as} (W=O) is not obvious in these composites, inferring the strong interaction between carbon and STA due to chemisorption through the formation of W-O-C bond. The composite Pt-Ru/STA-C has been analyzed by EDX analysis (Figure 4b). In addition to the Pt, Ru and C peaks, the results showed the peaks due to Si, W and O confirming the presence of STA. EDX analysis reveals that the atomic composition of Pt: Ru is 0.49: 0.51, which is close to 1:1 stoichiometry.

The crystal structures of all the composites were examined by XRD as shown in Figure 5. All the XRD responses represent the diffraction peaks of (111), (200), (220), and (311) planes, typical character of a Pt in face-centered cubic (fcc) phase. The diffraction peaks of the composites (Pt/C and Pt-Ru/C) produced by hydrogen reduction method were observed to be sharp with high intensity indicating high crystallinity (Figure 5a & c). On the contrary, very broad peaks with weak intensity were observed for STA containing composites (Pt/STA-C, Pt-Ru/STA-C), indicating they are not fully crystalline in nature (Figure 5b & d) as observed for the commercial Pt-Ru/C (J. M) (Figure 5e). The diffraction peaks of Pt-Ru nanoparticles in commercial Pt-Ru/C (Johnson Matthey), Pt – Ru/STA-C and Pt-Ru/C shifted to higher angles with respect to the diffraction lines of

pure Pt, indicating the decrease of lattice parameter. No evidence of peaks related to Ru was found in these catalysts. Compared with the diffraction peaks of Pt/C and Pt-Ru/C produced under hydrogen reduction method, peaks of the Pt/STA-C and Pt-Ru/STA-C shifted slightly to higher angles. This implies that there is some interaction between Pt or Pt-Ru particles with STA.

2. Ru supported on carbon (Ru/ STA-C) by POM reduction method

The FT-IR spectrum of Ru/ STA-C (Fig. 6a) shows the absence of band due to external (terminal) W=O indicating the strong interaction between carbon and STA due to chemisorption through the formation of W-O-C bond. The typical XRD pattern of Ru/ STA-C (Fig. 6b) shows a large diffuse peak at 42.9° and two small diffuse peaks at 42.28° (JCPDS: 06-663). Representative TEM images of 20% Ru/ STA-C can be seen in Fig.6c and d. It reveals that Ru nanoparticles are uniform in size and highly distributed on the carbon surface.

3. Ag-PANI-PMo_{12} nanocomposite (communicated to Nanoscale Research Letters)

The different stages of synthesis of the composites (Steps 1-2, Scheme 2) were monitored by UV-vis spectra (Fig.7). Figure 7a corresponds to the UV-vis spectrum recorded from PMo_{12} solution which has no obvious absorbance in the range 400-800 nm. Figure 7b corresponds to the UV- vis absorption of the blue colored solution containing PMo_{12} and aniline (step 1. Scheme 3); the presence of an absorption band at 700 nm can be seen and is characteristic of one-electron reduced PMo_{12} (electron is transferred from aniline to PMo_{12}). The produced d^1 metal ion of Mo is responsible for the d-d transition resulting in absorption in the visible region. Fig. 7c and 7d correspond to the spectra of PMo12-PAni solution to which $AgNO_3$ and $HAuCl_4$ solutions were added respectively (Step 2, Scheme 3); strong absorption bands at 450 and 573 nm due to the excitation of surface plasmon resonance on Ag and Au nanoparticle in Ag-PAni-PMo_{12} (Fig. 7c) and Au-PAni-PMo_{12} (Fig. 7) respectively were observed.

The presence of Ag and Au nanoparticles in Ag-PAni-PMo12 and Au-PAni-PMo12 was further confirmed by powder XRD measurements, as shown in Figure 8. The XRD pattern of Ag nanoparticles containing composite showed four strong bands with maximum intensity at 38.1°, 44.3°, 64.4°, 77.4°, and 81.5° representing Bragg's reflections from (111), (200), (220), (311), and (222) planes of the standard cubic phase

of Ag (Fig .8a). Au-PAni-PMo12 composite also exhibited the presence of four strong bands with maximum intensity at 38.1°, 44.3°, 64.5°, 77.5°, and 81.7° representing (111), (200), (220), (311), and (222) planes of standards cubic phase of Au (Fig .8b).

In order to confirm the presence of PAni and the phosphomolybdate anion in the composites, Fourier transform infrared (FTIR) analysis of the Ag-PAni-PMo_{12} and Au-PAni-PMo_{12} (Fig. 9a and b) nanocomposites were carried out. Both the composites showed the characteristic bands of PAni (marked with arrows), and bands assigned to the phospomolydate anion (marked with circles). The peak at 1575 cm^{-1} is assigned to a deformation mode of benzene rings, the one at 1488 cm^{-1} to a deformation of benzene or quinoide rings, the ones at 1248 cm^{-1} and 1147 cm^{-1} to a C = N stretching of a secondary amine, at 1060 cm-1 to a P-O bond, at 955 cm^{-1} to a Mo=O terminal bond, at 876 cm^{-1} to a vertex Mo-O-Mo bond, and finally at 800 cm^{-1} to an edge Mo-O-Mo bond.

The morphology of the prepared nanocomposites was examined using scanning electron microscopy (SEM). Fig. 10a and b show the SEM images of Ag-PAni-PMo_{12} and Au-PAni-PMo_{12} composites. However, the nanocomposites exhibited a highly microporous structure which is of great interest for their application as electrodes since it represents an optimization of the electrode-electrolyte interface.

Figure 11a & b shows typical low-magnification TEM images of the Ag-PAni-PMo_{12} composites. The spherical Ag nanoparticles are well distributed and stabilized by the polymer. The corresponding histogram (Figure 12a) of the size distribution of the Ag nanoparticles indicates a broad distribution ranging from 3.5nm to 9 nm of the Ag nanoparticles formed during the reaction. TEM images of Au-PAni-PMo_{12} composite (Figure 11c and 11d) shows most of the Au nanoparticles aggregated with a size distribution ranging from 4 to 9 nm (Fig. 12b). The particles are aggregated into dendritic structures composed of nanorod arms with an average diameter of ca 3 nm and length 10 nm and they were rather polydisperse. The detailed structure of the Ag and Au nanoparticles in the prepared nanocomposites were further revealed by high resolution TEM (Fig. 13). From Fig 13a it can be seen that the spherical silver nanoparticles core surrounded by PAni shell in the Ag-PAni-PMo_{12} composite and nanoparticles have clear crystalline planes aligned along a specific direction with a d spacing of 2.40 Å. Figure

13b indicated the dark Au nanorods arms surrounded by a grayish sheath-protected PAni in the Au-PANi-PMo_{12} composite. The planes of the rods aliened with d spacing of 2.38 Å.

4. 1. WO_3 nanorods (J. Rajeswari, B. Viswanathan and T. K. Varadarajan, Tungsten trioxide nanorods as supports for platinum in methanol oxidation, Materials Chemistry and Physics, 2007**)**

A schematic representation of the formation of WO_3 nanorods is shown in scheme.3. It shows the possible mechanism of tungsten trioxide nanorods formation. The precursor material is composed of the cationic surfactant group (tetrabutyl ammonium ion) and the anionic decatungstate ion, represented as octahedral units. Formation of the precursor can be understood as follows: The TBA^+ cations react with the tungsten oxide octahedra (scheme.3a) and forms lamellar aggregates (also supported from the SEM image Fig 15a) of the $((C_4H_9)_4N)_4W_{10}O_{32}$ in which the tungstate anions are encapsulated in the array of TBA groups. The TBA groups are suggested to behave as glue that holds the WO_6 octahedra together with spacing between different lamellar layers (scheme.3b). In the crystallization process, surfactant molecules may serve as a growth controller, as well as an agglomeration inhibitor, by forming an encapsulated layer. When heated at 450 °C for 2h, the structure directing, tetrabutylammonium group decomposes resulting in the formation of lamellar sheets of WO_3 (scheme.3c). On gradual increase of the pyrolysis duration to 3h these lamellar sheets were rolled onto themselves to form WO_3 nanorods (scheme.3d).

Figure 14a shows the XRD recorded for WO_3 nanorods synthesized by a single step pyrolysis of tetrabutylammonium decatungstate. All the peaks can be undisputedly indexed to monoclinic WO_3 (JCPDS: 75-2072). There are no peaks detected for other phases, indicating that single phase of WO_3 with high purity has been prepared. No peaks of impurities were detected from this pattern. The average crystallite sizes of the nanorods was calculated by using Scherrer's formula

$L = 0.89 \lambda / \beta \cos\theta$,

where, L is the average crystallite size, λ = 0.15418 nm for CuKα, β is the half maximum peak width and θ is the diffraction angle in degrees. The average crystallite sizes calculated by the Scherrer's formula along the (001), (020), (200), (021) and (220)

have values of about 36, 27, 34, 39 and 33 nm, respectively. The Raman spectrum (Fig. 14b) for the material shows characteristic O-W-O bending (260 and 334 cm^{-1}) and stretching modes (703 and 813 cm^{-1}) of WO_3. The typical morphology of the precursor compound, tetrabutylammonium decatungstate, $((C_4H_9)_4)N)_4W_{10}O_{32}$ and the as synthesized WO_3 are presented in the SEM images (Fig. 15a and b respectively). Fig. 15a displays the side view of the precursor compound revealing a lamellar aggregations. Fig. 15b presents the image of the as synthesized WO_3 showing the formation of nanorods. The rods are polydispersed with few hundred nanometers (100 – 500 nm) of length and 20-60 nm of width. Thus the findings indicate that the pyrolysis products are obtained from the $((C_4H_9)_4)N)_4W_{10}O_{32}$ microsheets and the synthesized material constitutes nanosized one dimensional tungsten oxide materials. Fig. 15c displays the SEM image of the WO_3 obtained from the pyrolysis of ammonium paratungstate, $(NH_4)_{10}H_2W_{12}O_{42}.XH_2O$. It can be seen that the material is composed of irregular particles of varying size with plate like morphology. From the SEM analysis, it is revealed that rod like morphology can be obtained only when tetrabutylammonium group is present in the precursor compound. SEM has also been employed to observe the morphology of the commercially obtained WO_3 (Fig 15d). It shows agglomerated microparticles with no specific morphology. TEM was also employed to provide further insight into structure and morphology of the as synthesized material. The morphologies of the products obtained after 2h and 3h were confirmed by the TEM images to be nanosheet (Fig. 16a) and nanorod (Fig. 16b and c) respectively. The sheet has a dimension of about 350 nm and 190 nm lateral size and thickness respectively. The dimensions of the nanorods vary in ranges 130-480 nm and 18-56 nm of length and width respectively. The high resolution TEM image of a nanorod is illustrated in Figure 16d. The lattice fringes are explicitly clear with d spacing of 0.375 nm for the (020) plane. There has been a strong correlation on the d value obtained from the HRTEM and XRD. The electron diffraction shown in the inset of Figure 4c indicates the crystallinity of the material. The EDAX (inset of Fig. 16c) results confirmed the presence of respective constituent elements in WO_3 nanorods. The copper signals originate from a copper supporting microgrid.

4.2. Pt /WO_3 and Pt/ WO_3-CNT (results unpublished)

The XRD pattern and high resolution TEM image of Pt loaded WO_3 nanorods are given in Fig. 17 (i) and (ii). The diffraction pattern corresponded to the reflections of monoclinic WO_3 nanorods and face centered cubic Pt (JCPDS card no.JCPDS 04-0802). The presence of platinum on the surface of WO_3 nanorods can be seen from Fig. b and the size of the Pt nanoparticles calculated is in the range of 4-6 nm. The XRD pattern and high resolution TEM image of Pt loaded on WO_3 nanorods and CNT composites are given in Fig. 17 (iii) and (iv). The diffraction pattern exhibited the peaks corresponding to Pt, WO_3 and CNT and the high resolution TEM image showed the dispersion of Pt nanoparticles on the composites. The inset of Fig. 17 (ii) and (iv) shows the EDX spectra of Pt /WO_3 and Pt/ WO_3-CNT with the signals due to the constituent elements of the electrocatalysts.

4.3 MoO_2 and MoS_2 nanorods (results unpublished)

The dimensions of the MoO_2 nanorods calculated from the TEM image (Fig. 18a) ranges in 5-10 μm length and 20- 50 nm width. The inset of Fig. 18a shows the EDAX signals due to Mo and O present in the nanorods. The XRD pattern (Fig. 18b) obtained is well in agreement with monoclinic MoO_2 (JCPDS no: 86-0135). The representative TEM image and XRD pattern of MoS_2 nanorods are shown in Fig.18c and d respectively.

4. 4. $Mo_xV_yO_z$ nanorods (results unpublished)

A distribution of nanorods of $Mo_xV_yO_z$ in high yields can be seen from the SEM image of $Mo_xV_yO_z$ nanorods (Fig. 19a). This observation is well consistent with TEM observations (Fig. 19b) which also showed rod like morphology. Further, the dimension of the nanorod calculated from the TEM image is 4μm and 0.25μm of length and width respectively. The inset in Fig. 19b presents a corresponding electron diffraction pattern of $Mo_xV_yO_z$ nanorods, thus indicating the crystallinity of $Mo_xV_yO_z$. The diffraction pattern (Fig. 19c) obtained is well in agreement with single crystalline MoO_3 (JCPDS

card no. 89-5108) and VO_2 (JCPDS: 76- 0678). The EDAX spectrum (Fig. 19d) shows the signals due to Mo, V and O which are constituent elements of the nanorods.

Applications

1. Methanol oxidation

(Methanol oxidation by Pt/STA-C & Pt-Ru/STA-C electrocatalysts are **communicated**)

(Methanol oxidation by Pt/WO_3 nanorods: J. Rajeswari, B. Viswanathan and T. K. Varadarajan, Tungsten trioxide nanorods as supports for platinum in methanol oxidation, Materials Chemistry and Physics, 2007 (in press)

(Methanol oxidation by Pt/WO_3 nanorods-CNT composite: Results unpublished)

The electrocatalytic activities for methanol oxidation of electrocatalysts prepared by POM reduction method (Pt/STA-C & Pt-Ru/STA-C) and hydrogen reduction method (Pt/C & Pt-Ru/C) were analyzed by cyclic voltammetry in an electrolyte of 1 M H_2SO_4 and 1 M CH_3OH at 25 mV/s. The cyclic voltammograms of Pt and Pt-Ru based composite electrodes are shown in Figures 20a and 6b respectively. The data obtained from cyclic voltammograms are listed in Table 1. For comparison, the cyclic voltammogram obtained for the methanol oxidation by the commercial Pt-Ru/C (J. M) is presented in Figure 20b (ii). It is seen from the Table 1 that the Pt/STA-C and Pt-Ru/STA-C showed better performance in terms of current density and mass activity when compared to Pt/C and Pt-Ru/C. The activity for methanol oxidation follows the order: Pt-Ru/STA-C > Pt-Ru/C (J.M) > Pt/STA-C > Pt-Ru/C > Pt/C. The experimental results highlight the better performance for methanol oxidation on Pt-Ru/STA-C electrocatalyst prepared by POM reduction method over commercially available 20% Pt-Ru/C (J. M) catalyst and electrocatalysts prepared by hydrogen reduction method. The ratio of the forward anodic peak current (I_f) to the reverse anodic peak current (I_b) can be used to describe the catalyst tolerance to accumulation of carbonaceous species [75-78]. A higher ratio indicates more effective removal of the poisoning species on the catalyst surface. The I_f/I_b ratios of Pt/STA-C and Pt-Ru/STA-C are 1.11 and 1.05 respectively, which are higher than that of Pt/C (0.80) and Pt-Ru/C (0.91), showing better catalyst tolerance of STA containing composites.

To test the tolerance towards poisoning and long-term performance of the Pt and Pt-Ru nanoparticles on the carbon support towards the methanol oxidation reaction, chronoamperometric studies have been performed in 1M H_2SO_4 solution containing 1M CH_3OH at constant potential 0.5 V for 3600 s (Figure 20c & 20d). Inspite of the initial high current density, there is a constant decay in the current with respect to time for Pt/C (Figure 20c (ii)) and Pt-Ru/C (Figure 20d (iii)) electrodes respectively and it has reached the minimum during the period of study. This indicates that these electrodes decay faster due to poisoning. On the other hand, for the STA containing electrodes, Pt/STA-C (Figure 20c (i)) and Pt-Ru/STA-C (Figure 20d (i)), the potentiostatic currents decrease rapidly at short reaction times. At long times, the rate of current decay is small and a steady state current is achieved. This suggests better CO tolerance of POM (STA) containing electrodes which is in agreement with the high I_f/I_b values.

The electrochemical activities of platinum loaded on WO_3 nanorods and WO_3 nanorods-Carbon nanotubes (CNT) composites was studied using cyclic voltammetry in the presence of 1M H_2SO_4 and 1M CH_3OH. The cyclic voltammograms of Pt loaded on WO3 nanorods, commercial 20% Pt- Ru/C (J. M) and Pt loaded on bulk WO_3 (Pt/bulkWO_3) are also presented in Figure. 21a, 21b and 21c respectively. The peak current densities and mass activities due to methanol oxidation for various WO_3 nanorods containing electrocatalysts are shown in Table.2. The catalyst activities can therefore be ranked in the following order: 40% Pt/WO_3-CNT> 20% Pt/WO_3-CNT> 20% Pt/WO_3 nanorods> 20% Pt-Ru/C (J. M) > 20% Pt/ bulk WO_3.

2. Electrochemical supercapacitors (J. Rajeswari, B. Viswanathan, T. K. Varadarajan, Supercapacitors based on tungsten trioxide nanorods, Indian Pat.No. 1488 CHE 07 and P. S. Kishore, B. Viswanathan and T. K. Varadarajan, Indian Pat. Appl.**)**

Considering the promising aspects of ruthenium oxide and polyoxometalates, an electrode material has been developed containing both ruthenium and polyoxometalates. The effective utilization of the active electrode material that is ruthenium has been achieved by decreasing the particle size of the ruthenium into nanometer range by using polyoxometalates and then dispersing them on carbon. The highly dispersed ruthenium nanoparticles reduced by silicotungstic acid (SiW_{12}) in the composite were

electrochemically oxidized to active pseudocapacitive oxide-hydroxide form of ruthenium by sweeping the voltage. The weight percentage of ruthenium on carbon has been varied as 10%, 20% and 40%, the corresponding specific capacity values obtained from the chronopotentiograms (Fig. 21A) are shown in Table.3. This shows that the specific capacitance of Vulcan XC-72R has been increased to a great extent by the loading of ruthenium nanoparticles in the composites. For comparison, the chronopotentiograms of 20% Ru loaded on carbon reduced by phosphomolybdic acid (PMo_{12}) and reduced under H_2 atmosphere have been given in Fig. 21B and the specific capacitance values obtained can be seen from Table. 3. The values demonstrate that the ruthenium nanoparticles reduced and stabilized by SiW_{12} showed a high specific capacitance than other systems. Fig. 21C, shows the voltammetric behavior of Ru-SiW_{12}/C composites with various weight percentage loadings of ruthenium. The composites showed increased capacitive behavior (reflected from the increased current values) with increment in the weight percentage of ruthenium. The stability of the electrodes was evaluated by conducting the charge-discharge cycling tests for 40 cycles. Figure 21D shows a decrease in capacitance for all the three electrodes; however the percentage loss is low for Ru-SiW_{12}/C electrode.

Figure 22a and b shows the chronopotentiograms obtained for tungsten trioxide nanorods and bulk WO_3 electrode at a constant current density of 3 mA/cm^2 in the potential range of 0.2 to -0.5 V in 1M H_2SO_4 electrolyte. The anodic peak current density of tungsten trioxide nanorods is $25mA/cm^2$ at a scan rate of 50 mV/s (Fig 22c). This value is 7.2 times higher than bulk WO_3 (3.5 mA/cm^2) indicating high capacitive nature of WO_3 nanorods than its bulk counterpart. The specific capacitance calculated from Fig. 22 a and b has been tabulated in Table. 4 and this demonstrates that further development in supercapacitor technology can be accomplished by moving from bulk to nanostructured materials.

3. Hydrogen evolution reaction (J. Rajeswari, P. S. Kishore, B. Viswanathan and T. K. Varadarajan, Nanoscale Research Letters, 2007, Article in press).

The linear sweep voltammograms of WO_3 nanorods and bulk WO_3 carried out in 1M H_2SO_4 at a scan rate of 5 mVs^{-1} in the potential range -0.2 to -0.8 V are shown in Figure 23a & b respectively. The bare glassy carbon electrode showed no activity towards hydrogen evolution as evident from the Figure 23c. At -0.8 V, the current densities of HER on WO_3 nanorods (23$mAcm^{-2}$) is higher than that of bulk WO_3 (15$mAcm^{-2}$) indicating the enhanced electrocatalytic activity of WO_3 nanorods. The kinetic parameters of the electrodes were determined from the Tafel plot as shown in Figure 24 and the data are summarized in Table 5. The Tafel plots show two well-defined linear regions for both bulk WO_3 as well as WO_3 nanorods. The slopes in the low current density region (region 1) for bulk WO_3 and WO_3 nanorods are -213 and -188 $mVA^{-1}cm^2$ respectively. The slopes are -30 and -25 $mVA^{-1}cm^2$ in the high current density region for bulk WO_3 and WO_3 nanorods respectively (region 2). The lower Tafel slope obtained for WO_3 nanorods in comparison to bulk WO_3 indicates the facile HER on WO_3 nanorods as the electrode. The exchange current densities calculated at -0.199 V (Ag/AgCl (Satd KCl)) for 1M H_2SO_4 solution provides information on the catalytic activity of the electrode for HER. The higher exchange current density value of WO_3 nanorods ($2.75x10^{-6}$ Acm^{-2}) when compared to bulk WO_3 ($8.57x10^{-7}$ Acm^{-2}) shows the better catalytic performance of WO_3 nanorods towards HER.

4. Oxygen reduction reaction (results unpublished)

The polarization curves for the oxygen reduction reaction of Pt/C and Pt/STA-C catalysts in O_2-saturated 0.5 M H_2SO_4 are shown in Fig. 25. The ORR activities calculated from the difference in the current density values of the electrodes in O_2 saturated and Ar saturated 0.5 M H_2SO_4 are given in Table. 6. This indicates that the Pt/C modified by STA have better electrocatalytic performance towards oxygen reduction reaction. A reasonable explanation is the high dispersion and uniform distribution of platinum particles on the carbon support. Moreover, the ability of STA containing electrodes to decompose the intermediate, hydrogen peroxide formed during oxygen reduction can also attributed to the high performance of Pt/STA-C catalysts.

Linear sweep voltammetric responses of WO_3-free (Curve a) and WO_3 nanorods-modified (Curve b) and bulk WO_3 modified (Curve c) Pt/C deposits on glassy carbon in O_2-saturated 0.5 M H_2SO_4 are shown in Fig. 26. WO_3 modified electrodes showed

higher electrocatalytic activity towards oxygen reduction reaction than the WO_3 free electrode. The high ORR activity (Table.7) exhibited by WO_3 nanorods than its bulk counterpart has demonstrated the superior electrocatalytic behavior of 1-D nanostructures than their bulk counterpart.

References

1. A. I. Abdelrahman, A. M. Mohammad, T. Okajima and T. Ohsaka, J. Phys. Chem. B 110 (2006) 2798.

2. G. Che, B. B. Lakshmi, C. R. Martin and E. R. Fisher, Langmuir 15 (1999) 750.

3. J. Zhang, M. Kambayashi and M. Oyama, Electrochem.Comm. 6 (2004) 683.

4. J. Hu, T. W. Odom, C. M. Lieber, Acc. Chem.Res. 32 (1999) 435.

5. P. J. Kulesza, B. Karwowskaa, B. Grzybowskaa, A.Wieckowski, Electrochimi. Acta 44 (1998) 1295.

6. J. Chen, M. Wang, B. Liu, Z. Fan, K. Cui and Yafei Kuang, J. Phys. Chem. B 110 (2006) 11775.

7. A.C.D. Angelo, Int J Hydrogen Energy 32 (2007) 542.

8.M. Wu, P. K. Shen, Z. Wei, S. Song and M. Nie, J. Power Sources 166 (2007) 310.

9. W. Yao, J. Yang, J. Wang and Y. Nuli, Electrochem. Commun 9 (2007) 1029.

10. W. Xu, X. Zhou, C. Liu, W.Xing , T. Lu, Electrochem.Commun. 9 (2007) 1002.

11. C. C. Hu, W. C. Chen, K. H. Chang, J.Electrochem. Soc. 151 (2004) A281.

12. J. P. Zheng, T. R. Jow, J. Electrochem. Soc. 142 (1995) L6.

13. H. Kim, B. N. Popov, J. Power Sources 104 (2002) 289.

14. E. Papaconstantinou Chem. Soc.Rev. 18 (1989) 1.

15. O. Savadogo, E. Ndzebet, Int. J. Hydrogen Energy 26 (2001) 213.

16.M. Chojak, M. Mascetti, R. Wlodarczyk, R. Marassi, K. Karnicka, K. Miecznikowski, P. Kulesza, J. Solid State Electrochem. 8 (2004) 854.

17. B. Keita, L. Nadjo, J. Haeussler, J. Electroanal. Chem. 243 (1988) 481.

Figures

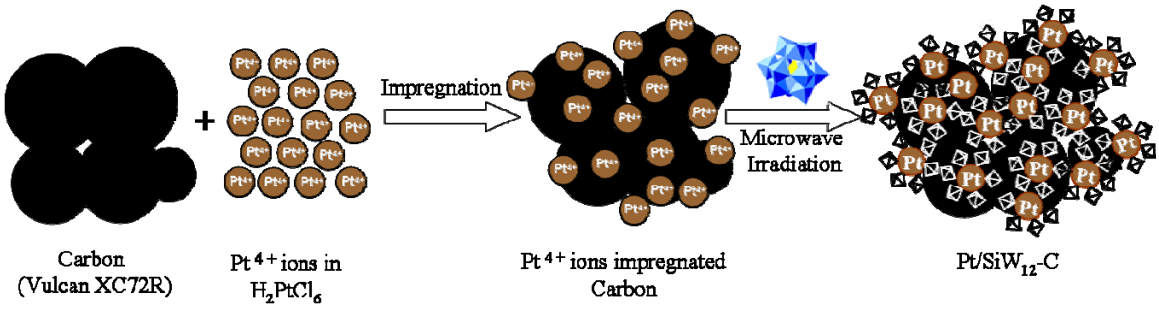

Scheme 1. Schematic representation of the preparation of carbon supported Pt nanoparticles by STA

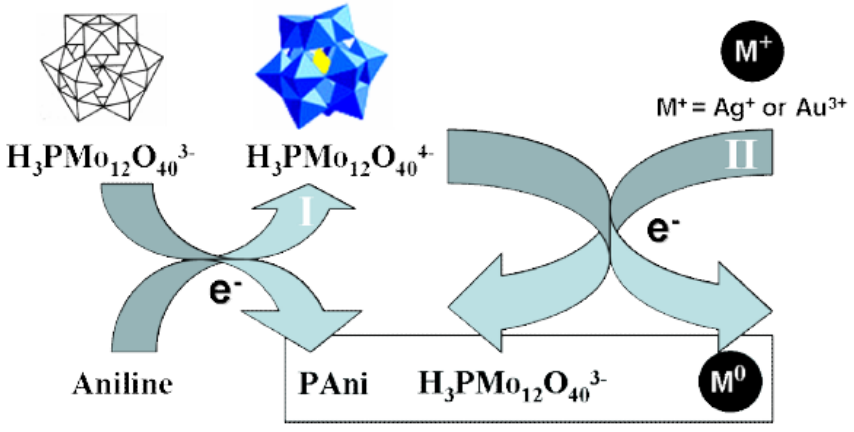

Scheme 2. Schematic representation of the PMo_{12} mediated synthesis of metal nanoparticle embedded PAni-PMo_{12} composites

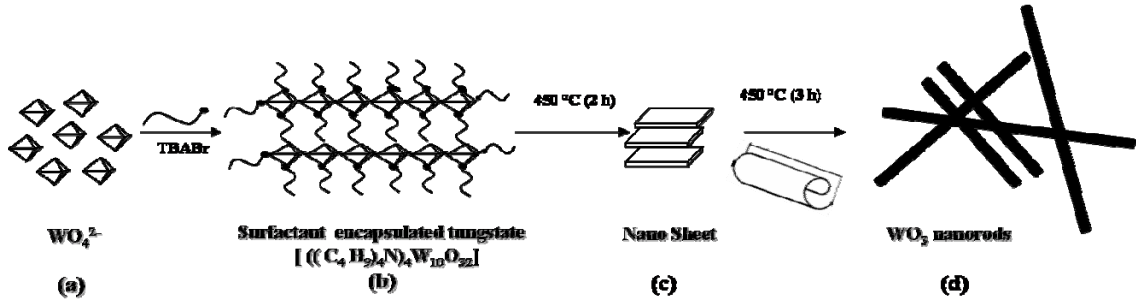

Scheme 3. Scheme for the formation of WO_3 nanorods

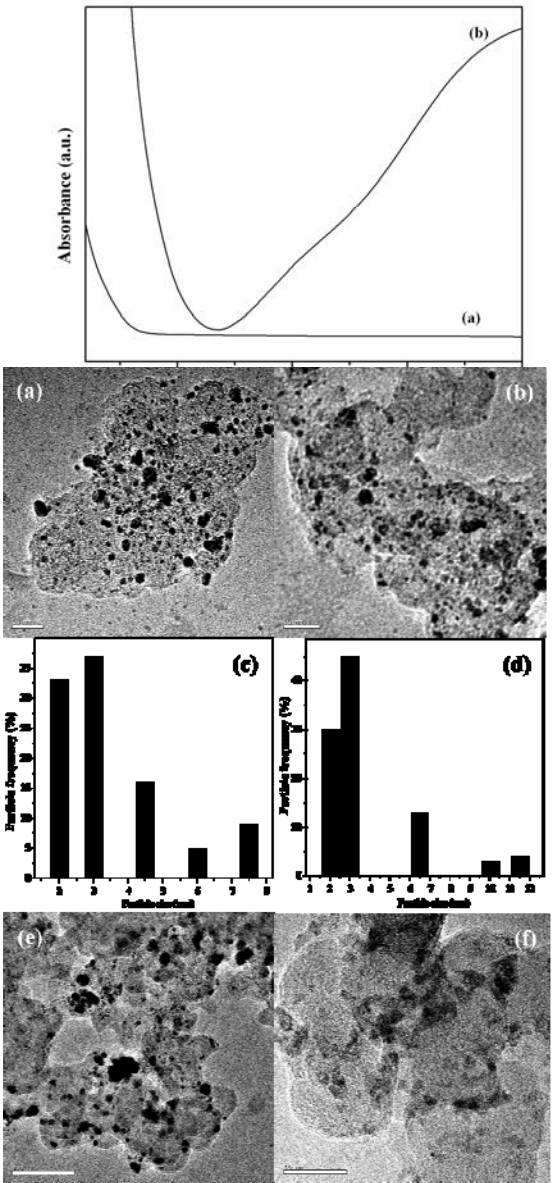

Figure 1. UV – vis spectra of (a) pure STA and (b) reduced STA

Figure 2. TEM images of (a) Pt/STA-C, (b) Pt- Ru/STA-C, (e) Pt/ C and (f) Pt- Ru/ C (c) and (d) represents particle size distribution obtained from (a) and (b) respectively

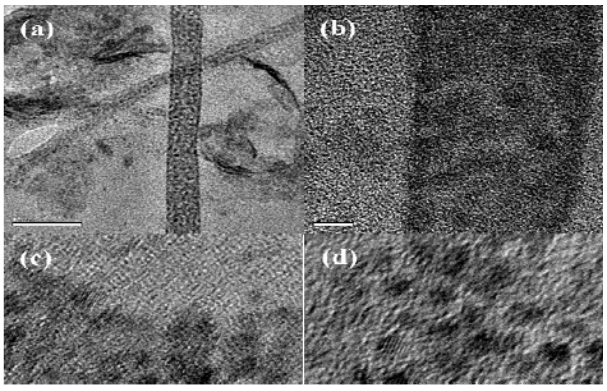

Figure 3. High Resolution TEM images of Pt/STA-C ((a), (b) & (c)) and Pt-Ru/STA-C (d)